

Enhanced H₂O formation through dust grain chemistry in X-ray exposed environments

R. Meijerink^{1,2}, S. Cazaux², and M. Spaans²

¹ Leiden Observatory, Leiden University, P.O. Box 9513, NL-2300 RA Leiden, Netherlands

² Kapteyn Astronomical Institute, PO Box 800, 9700 AV Groningen, The Netherlands
e-mail: meijerink@astro.rug.nl

Received ??; accepted ??

ABSTRACT

Context. The Ultra-luminous infrared galaxy Mrk 231, showing signs of both black hole accretion and star formation, exhibits very strong water rotational lines between $\lambda = 200 - 670 \mu\text{m}$, comparable to the strength of the CO rotational lines. High redshift quasars also show similar CO and H₂O line properties, while starburst galaxies, such as M82, lack these very strong H₂O lines in the same wavelength range, but do show strong CO lines.

Aims. We explore the possibility of enhancing the gas phase H₂O abundance in X-ray exposed environments, using bare interstellar carbonaceous dust grains as a catalyst. Cloud-cloud collisions cause C and J shocks, and strip the grains of their ice layers. The internal UV field created by X-rays from the accreting black hole does not allow to reform the ice.

Methods. We determine formation rates of both OH and H₂O on dust grains, having temperature $T_{\text{dust}} = 10 - 60 \text{ K}$, using both Monte Carlo as well as rate equation method simulations. The acquired formation rates are added to our X-ray chemistry code, that allows us to calculate the thermal and chemical structure of the interstellar medium near an active galactic nucleus.

Results. We derive analytic expressions for the formation of OH and H₂O on bare dust grains as a catalyst. Oxygen atoms arriving on the dust are released into the gas phase under the form of OH and H₂O. The efficiencies of this conversion due to the chemistry occurring on dust are of order 30 percent for oxygen converted into OH and 60 percent for oxygen converted into H₂O between $T_{\text{dust}} = 15 - 40 \text{ K}$. At higher temperatures, the efficiencies rapidly decline. When the gas is mostly atomic, molecule formation on dust is dominant over the gas-phase route, which is then quenched by the low H₂ abundance. Here, it is possible to enhance the warm ($T > 200 \text{ K}$) water abundance by an order of magnitude in X-ray exposed environments. This helps to explain the observed bright water lines in nearby and high-redshift ULIRGs and Quasars.

Key words. Galaxies: starburst, AGN; ISM: chemistry

1. Introduction

Warm molecular gas ($T > 100 \text{ K}$) cools mainly through CO, H₂O, and H₂ ro-vibrational transitions (Neufeld & Kaufman 1993; Neufeld et al. 1995). The ground state lines of CO, up to $J = 6 - 5$, are extensively studied from the ground in a large number of galaxies (see, e.g., Papadopoulos et al. 2010) up to a redshift $z \sim 0.04$. Unfortunately, the atmosphere makes it impossible to study CO transitions with $J > 8$ and H₂O rotational lines. It is these lines, however, that are tracing the warm molecular gas. Moreover, these lines are sensitive to extreme UV irradiation from star-formation and X-rays due to supermassive black-hole accretion. Some high- J CO lines have been observed in bright galactic objects such as the Orion Bar and Sagittarius A (cf. Hollenbach & Tielens 1999), and the Class 0 object L1448-mm (Nisini et al. 1999). It is only recently that significant progress is being made in the study of the warm molecular interstellar medium (ISM) in nearby galaxies. Both high- J as well as rotational water lines have been observed abundantly after the launch of the Herschel Space observatory, that is operating between wavelengths $\lambda = 55 - 672 \mu\text{m}$. The successful HerCULES open time key program has observed 29 close (U)LIRGs with both SPIRE and PACS instruments, revealing CO lines up CO $J = 14 - 13$ (while current follow-up PACS observations might detect even higher transition) and H₂O lines in Mrk 231 that are of comparable strengths (van der Werf et al. 2010;

González-Alfonso et al. 2010). These CO and H₂O lines are at least in part produced in regions of the galaxy exposed to X-rays, so-called XDRs (Maloney et al. 1996; Meijerink & Spaans 2005), but emission produced through shock excitation may also contribute as observed for OH in Mrk 231 (Fischer et al. 2010). Moreover, *Herschel*-PACS also detected a lot of high- J CO lines as well as H₂O and OH in embedded objects, such as DK Chamaeleontis (van Kempen et al. 2010) and in disk atmospheres, e.g., HD 100546 (Sturm et al. 2010), where X-rays also affect the chemical-thermal structure. Even though this paper focuses on an application to ULIRGs, it will have applications to other objects as well.

Understanding the excitation and chemistry of these important molecules is therefore key in studying the dominant physical processes in the ISM and star-formation. CO is a linear molecule, and the radiation transfer models allow to calculate far-infrared to millimeter spectra relatively easy for a given physical structure. Models predicting CO emission, where both the thermal-chemical structure and radiation transfer are calculated simultaneously have more problems to reach agreement. The case for H₂O is even worse, due to its complex nature: high critical densities $n_{\text{crit}} > 10^8 - 10^{10} \text{ cm}^{-3}$ in combination with high opacities, infrared-pumping and maser activity, makes an excitation calculation extremely challenging. Also, the excitation state in which water will enter the gas-phase after desorption or evaporation from a dust grain is very uncertain. A first

guess in this would be to divide the excess energy over the levels using equipartition, so 1/3 translational, 1/3 rotational and 1/3 vibrational excitation, with a Boltzmann distribution for the sub-levels. The formation of molecular hydrogen, H₂, in the ISM has been a long-standing problem. At extremely low metallicities, when no dust is present, H₂ either forms through the H⁻ route ($\text{H}^- + \text{H} \rightarrow \text{H}_2 + \text{e}^-$; Glover 2003; Launay et al. 1991), or through a three-body reaction ($\text{H} + \text{H} + \text{H} \rightarrow \text{H}_2 + \text{H}$). The three-body reaction dominates at very high densities ($n > 10^9 \text{ cm}^{-3}$; Galli & Palla 1998). For normal ISM conditions, H₂ is predominantly formed on dust grains, and much progress has been made over the past two decades, both experimentally as well as theoretically, in understanding this (much faster) formation of H₂ on the surfaces of grains (Pirronello et al. 1999; Katz et al. 1999; Cazaux & Tielens 2002; Zecho et al. 2002; Cazaux & Tielens 2004; Sha et al. 2005; Hornekar et al. 2006; Morisset et al. 2004; Cuppen et al. 2010b, and references therein). In general, the understanding is that CO is formed in the gas-phase, but the origin of gas-phase water is not so clear-cut. It is possible to form water in the gas-phase through either a chain of neutral-neutral reactions containing a number of temperature barriers, or through ion-molecule reactions when the gas is moderately ionized ($x_e \sim 10^{-5}$). The formation of water on interstellar dust can also be an efficient route in diffuse and dense clouds (Cuppen & Herbst 2007; Cuppen et al. 2010a). Several routes to form water can be considered, involving successive hydrogenation of oxygen either with H₂ or H. Because species can stay on the dust, they can repetitively collide with each other and react, even if there is an important barrier for the reaction to occur. In this case, dust grains provide a favorable place for improbable reactions (with high barriers) to occur (Cazaux et al. 2010). Also, other routes to form water, involving O₂ (Miyachi et al. 2008; Ioppolo et al. 2010) and O₃ (Mokrane et al. 2009) have been investigated and can be important at high dust temperatures ($T_{\text{dust}} > 20 - 30 \text{ K}$). The molecules present on the surface can be released in the gas phase through several mechanisms: desorption upon formation if the reaction is exothermic; photo-dissociation of surface species can lead to the desorption of products in the gas (i.e., photodissociation of H₂O leads to OH and H in the gas phase, Andersson et al. 2006); evaporation of the surface when the dust temperature is high enough (this process depends on the binding energy of the species). If many water molecules are formed and stay on the dust, then ices can be made. The bonds that hold the water molecules together are very strong (creating water clusters). As a result, when one or more monolayers of ice are formed on the grain, shocks will be the only effective way to remove the ice from grains (e.g., Draine 1995). It is thus only possible to have efficient formation of gas-phase water with grains as catalyst, when the grains are (close to) bare.

Objects such as Mrk 231 have very violent environments in the central regions around the super-massive black hole. This particular object has a derived $8 - 1000 \mu\text{m}$ infrared luminosity $L_{\text{IR}} = 4.0 \times 10^{12} L_{\odot}$ (Boksenberg et al. 1977). A highly absorbed power-law X-ray spectrum was observed by Braitto et al. (2004). It is in these extreme environments, that we expect cloud-cloud collisions to cause C and J shocks, and strip the grains of their ice layers. The internal UV field created by X-rays from the accreting black hole does not allow to reform the ice. The abundances of H₂O ($x_{\text{H}_2\text{O}} \sim 10^{-6}$, González-Alfonso et al. 2010) in the warm molecular gas of Mrk 231 are high. Here we study the effect of OH and H₂O formation on **bare** dust grains in environments with strong X-ray radiation fields, in order to investigate whether this process would be able to significantly boost the to-

tal production rate of these species in these environments. Our work differs from Hollenbach et al. (2009), since we consider an additional process to release molecular species into the gas phase, and also since our study only considers bare interstellar dust grains. Even though this paper focuses on an application to ULIRGs, it will have applications to other objects as well, such as X-ray irradiated disks around Young Stellar Objects. The manuscript is articulated in the following way: We first derive analytical expressions for the formation rates of OH and H₂O on dust grains. Then we compare these rates to the neutral-neutral gas-phase formation processes. Finally, the effects of the grains surface chemistry on the XDR thermo-chemical structure are shown. Their implications to explain recent observations with the *Herschel* Space Observatory are also discussed.

2. H₂O and OH formation rates

As mentioned earlier, gas-phase OH and H₂O can occur through neutral-neutral reactions, or when the medium is moderately ionized, $x_e \gtrsim 10^{-5}$, through ion-molecule reactions. The neutral-neutral reactions $\text{OH} + \text{H}_2 \rightarrow \text{H}_2\text{O} + \text{H}$ and $\text{O} + \text{H}_2 \rightarrow \text{OH} + \text{H}$ are slow at low temperatures, because they have activation barriers (Wagner & Graff 1987), and only contribute at temperatures $T > 250 - 300 \text{ K}$. The other route is $\text{H}^+ + \text{O} \rightarrow \text{O}^+ + \text{H}$, $\text{O}^+ + \text{H}_2 \rightarrow \text{OH}^+ + \text{H}$, $\text{OH}^+ + \text{H}_2 \rightarrow \text{H}_2\text{O}^+ + \text{H}$, $\text{H}_2\text{O}^+ + \text{H}_2 \rightarrow \text{H}_3\text{O}^+ + \text{H}$, followed by recombination $\text{H}_3\text{O}^+ + \text{e}^- \rightarrow \text{H}_2\text{O} + \text{H}$.

In our current X-ray chemistry code, only the grain surface reaction is taken into account for the formation of H₂. In order to study the effect of OH and H₂O molecule formation on grain surfaces, similar reactions for these species will be added to the chemical network

$$\frac{dn(\text{OH})}{dt} = n(\text{O})v_{\text{O}}n_{\text{dust}}\sigma\epsilon_{\text{OH}}, \quad (1)$$

$$\frac{dn(\text{H}_2\text{O})}{dt} = n(\text{O})v_{\text{O}}n_{\text{dust}}\sigma\epsilon_{\text{H}_2\text{O}}, \quad (2)$$

where ϵ_{OH} and $\epsilon_{\text{H}_2\text{O}}$ are efficiencies for the formation of OH and H₂O, respectively, and v_{O} the velocity of oxygen atoms. The expression for the efficiencies will be determined in the next section, where we calculate what fraction of an accreted oxygen atom is converted in gas phase OH or H₂O. Two different grain size distributions are considered, an MRN (Mathis et al. 1977) distribution and a Weingartner & Draine (2001) distribution, with $n_{\text{dust}}\sigma/n(\text{H}) = 10^{-21} \text{ cm}^{-2}$ and $2.8 \cdot 10^{-21} \text{ cm}^{-2}$, respectively. The MRN distribution considers a minimum dust grain size of 50 \AA , while Weingartner and Draine (W&D) consider much smaller grains, which are actually PAHs, and can be as small as 5 \AA . The W&D grain size distribution, however, seems more appropriate to environments such as the central regions of Mrk231, where dust grains can break in smaller particles due to, e.g., shocks. A larger cross section yield more enrichment of the medium with water and OH. The efficiencies are derived in the next section.

3. Grain surface chemistry

In this study, we consider carbon grains (graphite and carbonaceous). In order to describe the population of a certain species on a grain, we need to consider additional processes apart from the reactions that normally occur in the gas phase, such as neutral-neutral reactions. These are: accretion to, evaporation from, tunneling and thermal hopping of atoms and molecules on the surface of dust grains.

Table 1. Binding energies (in K) for carbon grains

Physisorption		
H	550	Bergeron et al. (2008)
O	1390	Bergeron et al. (2008)
H ₂	600	Akai & Saito (2003)
OH	1360	Cuppen & Herbst (2007)
O ₂	1440	Cuppen & Herbst (2007)
H ₂ O	2000	Cuppen & Herbst (2007)
O ₃	2240	Lee et al. (2009)
HO ₂	2160	Cuppen & Herbst (2007)
H ₂ O ₂	2240	Cuppen & Herbst (2007)
Chemisorption:		
H	8500	Jeleva et al. (2008)

Species arriving from the gas phase arrive at a random time and location on the dust surface. The arrival time depends on the accretion rate, which can be written as

$$R_{acc} = n_X v_X \sigma S_X \quad (3)$$

where n_X and v_X are the densities and velocities, respectively, of the species X , and σ is the cross-section of the dust particle. S_X is the sticking coefficient of the species with the dust, and we consider $S_X = 1$. The species X can go back to the gas phase through evaporation. This rate can be written as

$$R_{evap} = v_i \exp(-E_X/kT) \quad (4)$$

with v_i is the oscillator factor of atom in site i (which is of order 10^{12} s^{-1} for physisorbed atoms), and E_X the binding energy of species X (see Table 1 for the adopted values). The binding energy E_X can be either weak (for atoms and molecules) or strong (only for atoms). In this study we consider binding energies similar to those in Cazaux et al. (2010). There are two types of interactions between the atoms and the surface: a weak one, called physisorption (van der Waals interaction), and a strong one, called chemisorption (covalent bound). Atoms from the gas phase can easily access the physisorbed sites and become physisorbed atoms. These weakly bound atoms can travel on the surface at very low dust temperatures, meeting each other to form molecules. Moving of species on dust grains occurs through tunneling or thermal hopping (Cazaux & Tielens 2004). The mobility of a species X moving from physisorbed sites to physisorbed sites can be written as:

$$\alpha_{pp}(X) = v P_{pp}(X), \quad (5)$$

where $P_{pp}(X)$ is the probability for the atom to move from a physisorbed to another physisorbed site. In this study, we consider a range of surface temperatures $T > 15 \text{ K}$. At these temperatures, thermal hopping dominates and the probability for a species X to go from a physisorbed site to another physisorbed site can be written as:

$$P_{pp}(X) = \exp(-E_{pp}(X)/kT), \quad (6)$$

where $E_{pp}(X)$ is the barrier between to physisorbed sites, that we assume to be $2/3$ of the binding energy E_X (see Table 1). Hydrogen atoms that are physisorbed can also enter chemisorbed sites through tunneling effects or thermal hopping. Because of

the high barrier against chemisorption Sha (2002), H atoms usually tunnel through the barrier to populate chemisorbed site. The mobility for the H atoms can be written as:

$$\alpha_{pc} = v P_{pc}, \quad (7)$$

where $P_{pc}(H)$ is the probability for a physisorbed H atom to enter a chemisorbed site (Cazaux & Tielens 2004). Once two species meet in the same site, they can form a new species if the activation barrier for the formation can be overcome. According to the exothermicity of the reaction, the newly formed species is *directly released into the gas phase*. This probability, called f_{des} in this work, has been discussed in Cazaux et al. (2010), and is the most important route to release products to the gas-phase. Species present on the surface can also receive a UV photon and become photo-dissociated. In X-ray exposed environments, an internal UV field is created by excitation of Lyman-Werner bands, and about 30 percent of the locally absorbed X-ray is converted into UV (Maloney et al. 1996). The photo-dissociation of H₂O on the dust can lead to the release in the gas phase of the two products of the dissociation, OH and H. This mechanism has a very small chance to occur (2 percent, Andersson & van Dishoeck 2008). Although this process is much faster than thermal desorption (the grains are too cold to make thermal desorption efficient), it is not the main contributor in delivering species to the gas-phase. On grains, where ice layers are present, the desorption upon formation is less prominent, because the species are more strongly bound to the surface. In those environments, photo-desorption is the dominant route to release species into the gas phase. More details about the adopted reaction rates can be found in Cazaux et al. (2010). As we are interested in the oxygen chemistry, we will consider H, H₂, O, OH, O₂, H₂O, O₃, HO₂, and H₂O₂ as grain surface species in the chemical network.

Two different numerical methods are performed to follow the formation of species on dust grain surfaces: (1) a Monte Carlo and (2) a rate equations method. MC simulations are performed at several fixed dust temperatures. These calculations are very time consuming, and are used in order to check for which conditions the chemistry occurring on the dust enter the stochastic regime. The rate equations method is used to simulate the chemistry occurring onto dust for a wide range of dust and gas temperatures, gas phase chemical composition, radiation fields. This method is orders of magnitude faster than MC simulations.

3.1. Monte Carlo method

We use step-by-step Monte Carlo simulations to follow the chemistry occurring on dust grains. The dust grains are divided into square lattices of 10×10 adsorption sites. Each site on the grid corresponds to a physisorbed site and a chemisorbed site, so that the grain can be seen as two superimposed grids. Species originating from the gas phase arrive at a random time and location on the dust surface. This arrival time depends on the rate at which gas species collide with the grain (Eq. 3). When a species arrives at a point of the grid, it can become physisorbed, or, if its chemisorption states exists and its energy is high enough to cross the barrier against chemisorption, it becomes chemisorbed. In our model, however, because of the high barrier to access chemisorbed sites, H atoms mostly arrive from the gas phase in physisorbed sites. The species present on the surface may return to the gas phase if they evaporate (Eq. 4). The species that arrive at a location on the surface can move randomly across the surface by means of tunneling effects and thermal hopping

(Eq. 5). Species present on the surface can also receive a UV photon and become dissociated at the rates shown in table A.1. Once a chemical species present on the dust moves, or adsorbs a photon, or meets another species, the next event that occurs to this species is determined as well as its time of occurrence. Therefore, the events that concern every species on the dust are ordered by time of occurrence, and for each event that occurs, a next event for the concerned species is determined. In figure 1, we follow the fraction of oxygen that is released in the gas under the form of OH and H₂O for environments 1, 2, 4 and 5 (see Table 2 for adopted parameters). The parameters of these environments represent typical ambient low and high densities and radiation fields in the ISM of active galaxy centers, and are similar to those in Meijerink & Spaans (2005). The solid and dashed lines show our results for $T_{\text{dust}} = 20$ and 30 K respectively. For each environments, 50-60 % (30-40%) of the oxygen arriving on the dust goes back in the gas phase under the form of H₂O (OH). At higher dust temperatures ($\sim 35 - 40$ K), on the other hand, species coming on the dust evaporate very fast. Therefore, the efficiencies decrease dramatically since the grain surfaces are only sporadically covered by species.

3.2. Rate equations method

The rate equations method can be applied when there is a minimum coverage of 1 atom on the dust. This condition is satisfied if the grains are not too warm, that species can encounter each other before evaporating. By comparing our rate equations results with Monte Carlo simulations, we will define a range of dust temperatures for which rate equations are valid.

The rate equation method couples the different equations for the different species on the dust. The processes described in the previous subsection are dependent on the dust and gas temperature, UV field, and exo-thermicity of the reaction occurring on the dust. The equation for species X can thus be written as follows:

$$\frac{dn(X)}{dt} = n_{\text{gas}}(X)v_X N_s - n(X)n(Y)\alpha_{pp}(X) + (1 - f_{\text{des}})n(Y)n(Z)\alpha_{pp}(Y) - R_{\text{evap}_X}n(X) - R_{\text{phot}_X}n(X) + R_{\text{phot}_Y}n(Y) \quad (8)$$

where $\alpha_{pp}(X)$ and $\alpha_{pp}(Y)$ are the mobilities of the species X and Y (see Eq. 5). The different terms of this equation present (1) accretion of species X from the gas phase, (2) the formation of the new species that involve species X , (3) creation of the species X by the encountering of species Y and Z that stay on the surface, (4) evaporation of species X , (5) photo-dissociation of X on the dust, and (6) the creation of X by photo-dissociation of species Y .

3.3. Efficiencies derived from rate equation method

The formation efficiency is defined as the fraction of oxygen $f(\text{O})$ that is released in the gas phase under the form of another species. We studied this in a few different environments, chosen such that they resemble the conditions as found in the XDR models of Meijerink & Spaans (2005). The gas temperature is fixed at a constant temperature $T = 100$ K, and dust temperatures ranging from $T_{\text{dust}} = 10 - 60$ K. Four different radiation fields were considered at two fixed densities, $n = 10^3$ and $10^{5.5} \text{ cm}^{-3}$, in both the atomic and molecular regime. The parameters used are summarized in Table 2.

Table 2. Models parameters

Env.	n_{H}	$x(\text{HI})$	$x(\text{H}_2)$	$x(\text{OI})$	G_0
1	10^3	1	10^{-3}	3.4×10^{-4}	$10^0, 10^1, 10^2, 10^3$
2	„	10^{-1}	0.45	„	„
3	„	10^{-2}	0.5	„	„
4	$10^{5.5}$	1	10^{-3}	„	$10^3, 10^4, 10^5, 10^6$
5	„	10^{-1}	0.45	„	„
6	„	10^{-2}	0.5	„	„

In Figs. 2 and 3, we show the obtained efficiencies for OH and H₂O. The figures show that between dust temperatures $T_{\text{dust}} \sim 15 - 35$ K, the efficiencies for OH and H₂O are roughly constant. In this regime most of the oxygen goes to H₂O. For dust temperatures $T_{\text{dust}} \gtrsim 35 - 45$ K, the total efficiency for forming molecules is rapidly decreasing, and most of the atomic oxygen will not react to another species, before it evaporates from the grain. Therefore, the dust surface chemistry can only be effective, when the dust temperatures are not too high. Recall that the way to form OH and H₂O is through $\text{O} + \text{H} \rightarrow \text{OH}$ and $\text{OH} + \text{H} \rightarrow \text{H}_2\text{O}$. For slightly higher dust temperatures, the chance of an OH molecule to evaporate from the grain becomes higher than that for meeting another H atom. Therefore at temperatures $T_{\text{dust}} \gtrsim 35 - 40$ K, most of the oxygen atoms are incorporated into OH, and then ϵ_{OH} is highest.

Increasing the radiation field, has a similar effect as increasing the dust temperature, i.e., it results in a lower $\epsilon_{\text{H}_2\text{O}}/\epsilon_{\text{OH}}$ ratio, which is caused by photo-dissociation of H₂O on the surface. The strongest effect is seen in the environments 3 and 6, where the dominant hydrogen fraction is contained in H₂. In this environment, the hydrogen accretion rates are lowest, and thus also have the lowest atomic surface density on grains. When most of the gas is in atomic form, the hydrogen accretion is such that at high dust temperatures most of the oxygen is converted into OH. However, when the gas become more and more molecular, the atomic hydrogen accretion rate onto the dust decreases, and a larger fraction of atomic oxygen ends up in O₂. In environment 3, this is even the most likely product at temperature $T_{\text{dust}} > 35$ K.

In Figs. 4 and 5, the efficiencies for the formation of O₂, O₃, OH₂, and H₂O₂ are shown. The efficiencies for these species show a peak at dust temperatures $T_{\text{dust}} = 35 - 40$ K. The maximum efficiency for producing O₂ ranges from $\sim 10^{-2}$ in the atomic gas to $\sim 10^{-1}$ in molecular gas, and generally the efficiencies for other species are smaller. At temperatures $T > 40$ K, O₂ efficiencies dominate over those for OH, but this is the regime where efficiencies for the formation of molecular species become very small.

3.4. Validity of rate equation method

In order to estimate the uncertainties in the MC calculation, and to check for consistency between the MC and rate equation method, we did two additional MC simulations at dust temperatures of 20, 30, and 35 (low density) and 40 (high density). After a time t of $\sim 1000 - 2000$ years (low density) and $\sim 5 - 10$ years (high density), the efficiencies are converged and oscillate around a stable value. At $T_{\text{dust}} = 20$ and 30 K, the H₂O efficiencies vary between 0.5 to 0.6, and those for OH between 0.3 to 0.4, and thus very similar to the rate equation method. At

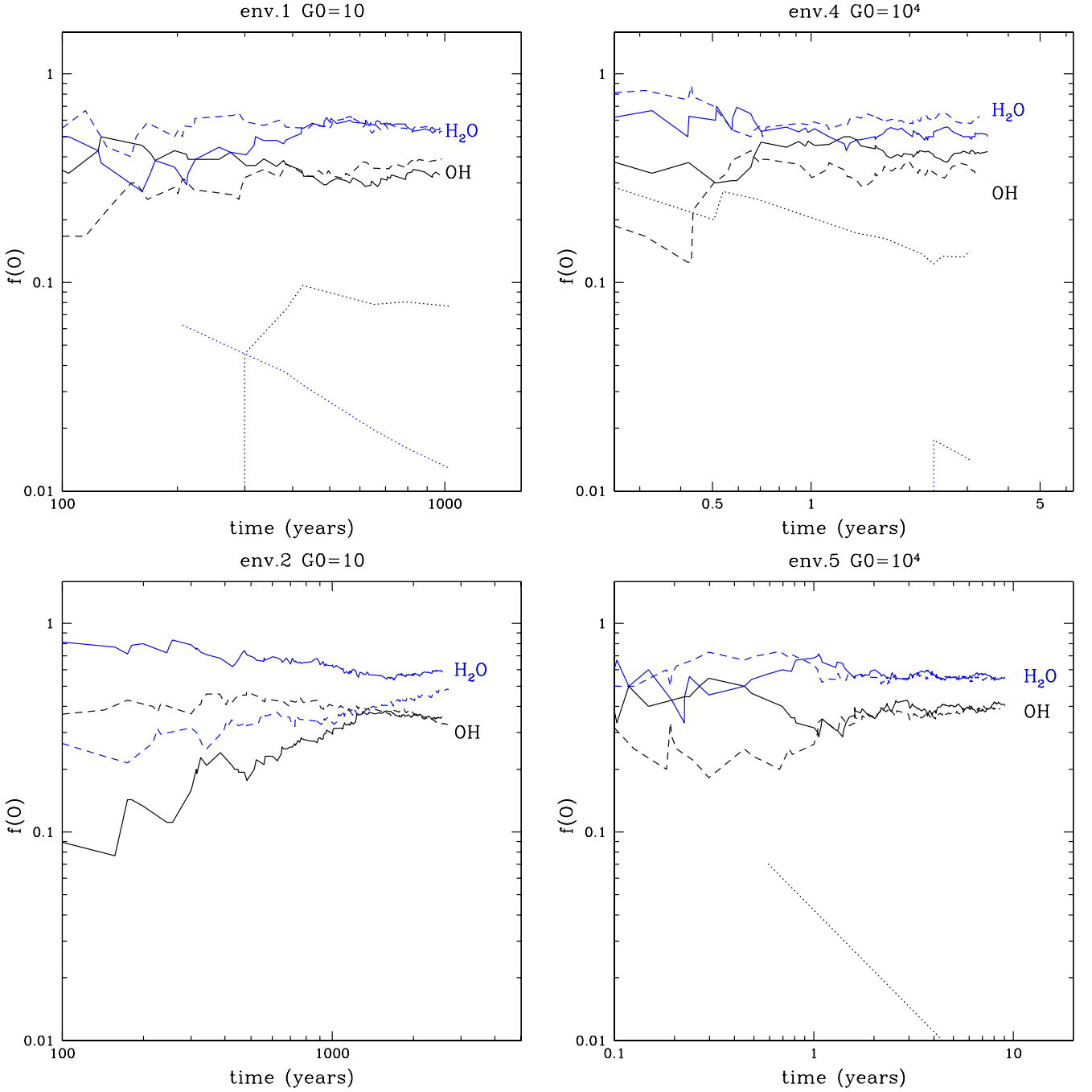


Fig. 1. Results of our Monte Carlo simulations on a 10×10 sites grain (30 \AA) for environments 1, 2, 4 and 5. The solid lines represent our results for $T_{\text{dust}} = 20 \text{ K}$, dashed lines for $T_{\text{dust}} = 30 \text{ K}$ and dotted lines $T_{\text{dust}} = 35 \text{ K}$ (left panel) 40 K (right panel).

the higher dust temperatures (35 and 40 K), the values obtained in the MC method are lower. The rate equations method is overestimating the efficiencies, and we are entering the stochastic regime.

We only concentrate on dust temperature $T_{\text{dust}} > 10 - 15 \text{ K}$. At very low dust temperatures, OH and H₂O are still able to form at a smaller efficiency, but the chemistry is different then for a number of reasons: (1) ices can form on the surface (2) the chemistry is different, because the binding energies are different, and (3) the surface of the grain will be saturated with H₂.

4. Analytical expressions for OH and H₂O formation efficiencies

The rate equations method gives the populations of the different species on the dust surface, which allows us to derive simplified analytic expression for formation efficiencies of OH and H₂O, that is easy to use in numerical codes. This means that the smallest set of reactions needed to reproduce the derived efficiencies from the rate equation calculation is determined. Although the analytic expression of the efficiencies is derived in Appendix A, the dependencies are given here:

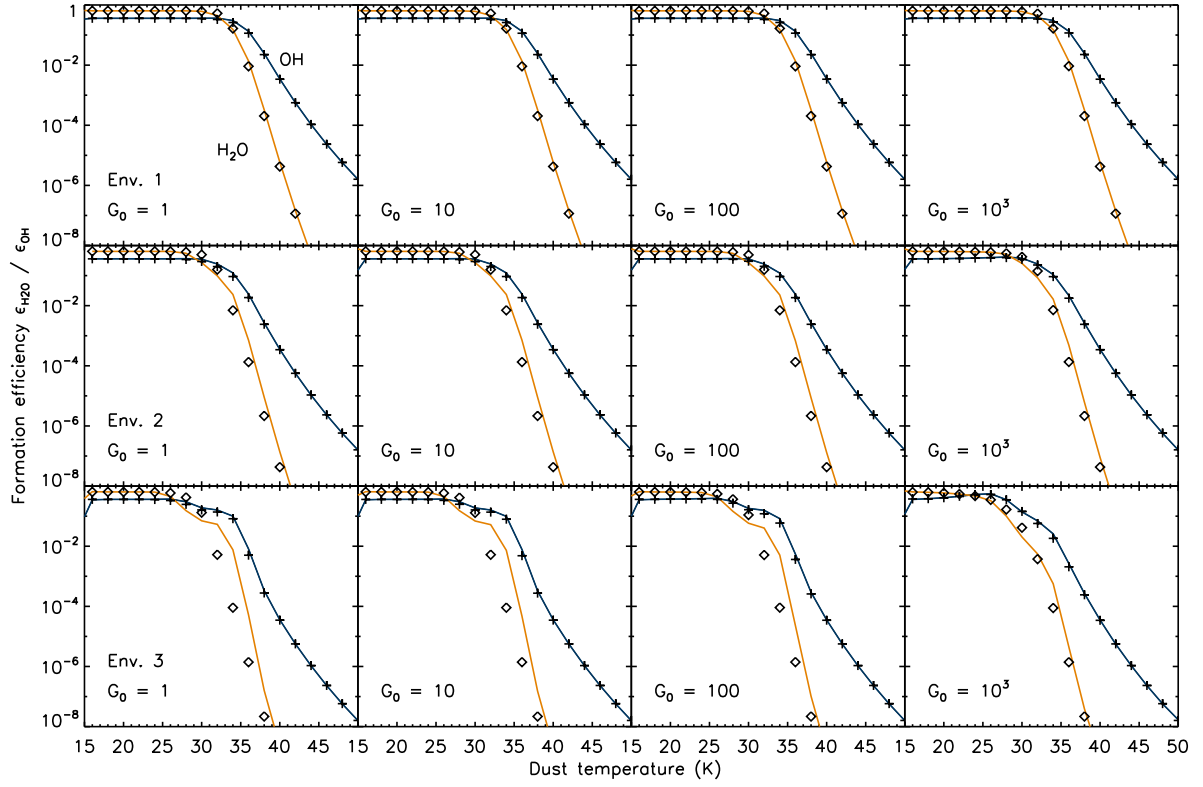


Fig. 2. Efficiencies for the formation of OH and H₂O in low density gas ($n = 10^3 \text{ cm}^{-3}$), in atomic and molecular hydrogen dominated gas. UV fields ranging from $G_0=1$ to 1000 are considered. Results from rate equation are shown by a solid and a dotted line for OH and H₂O, respectively. The analytical fit is shown by the crosses (OH) and diamonds (H₂O).

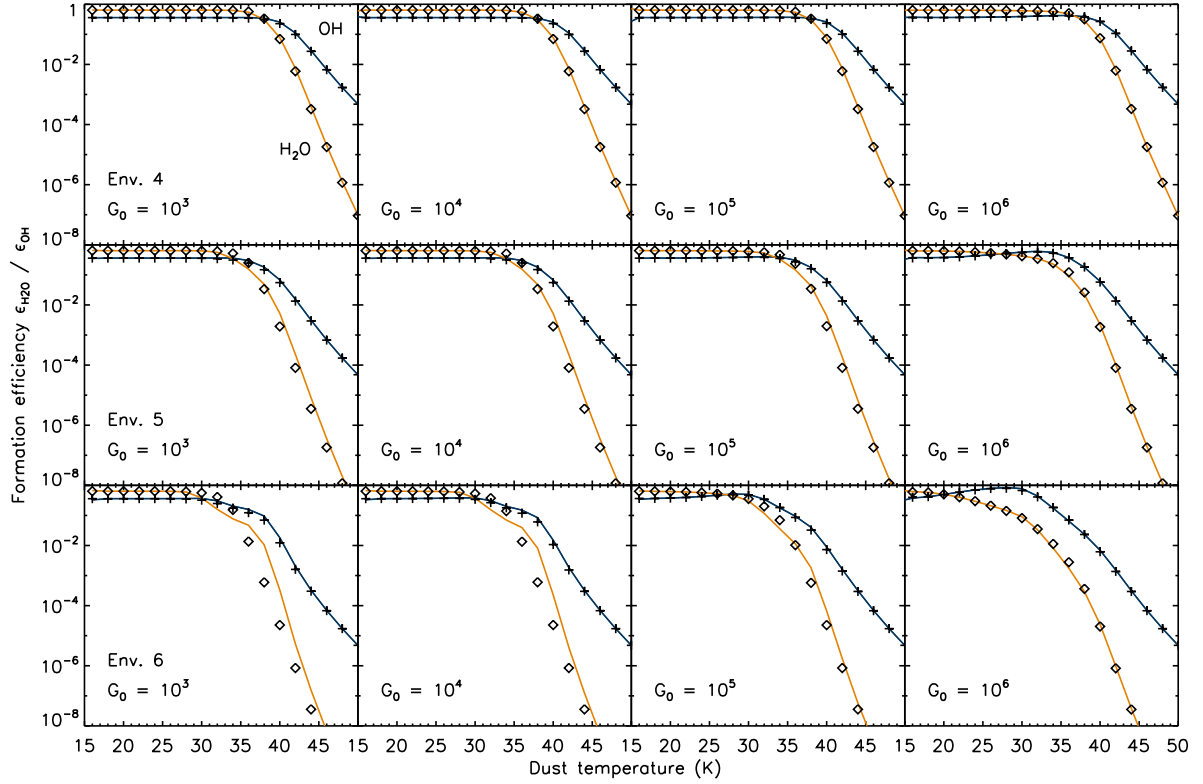


Fig. 3. Efficiencies for the formation of OH and H₂O in high density gas ($n = 10^{5.5} \text{ cm}^{-3}$), in atomic and molecular dominated gas. UV fields ranging from $G_0 = 10^3$ to 10^6 are considered. Results from rate equation are shown by a solid and a dotted line for OH and H₂O, respectively. The analytical fit is shown by the crosses (OH) and diamonds (H₂O).

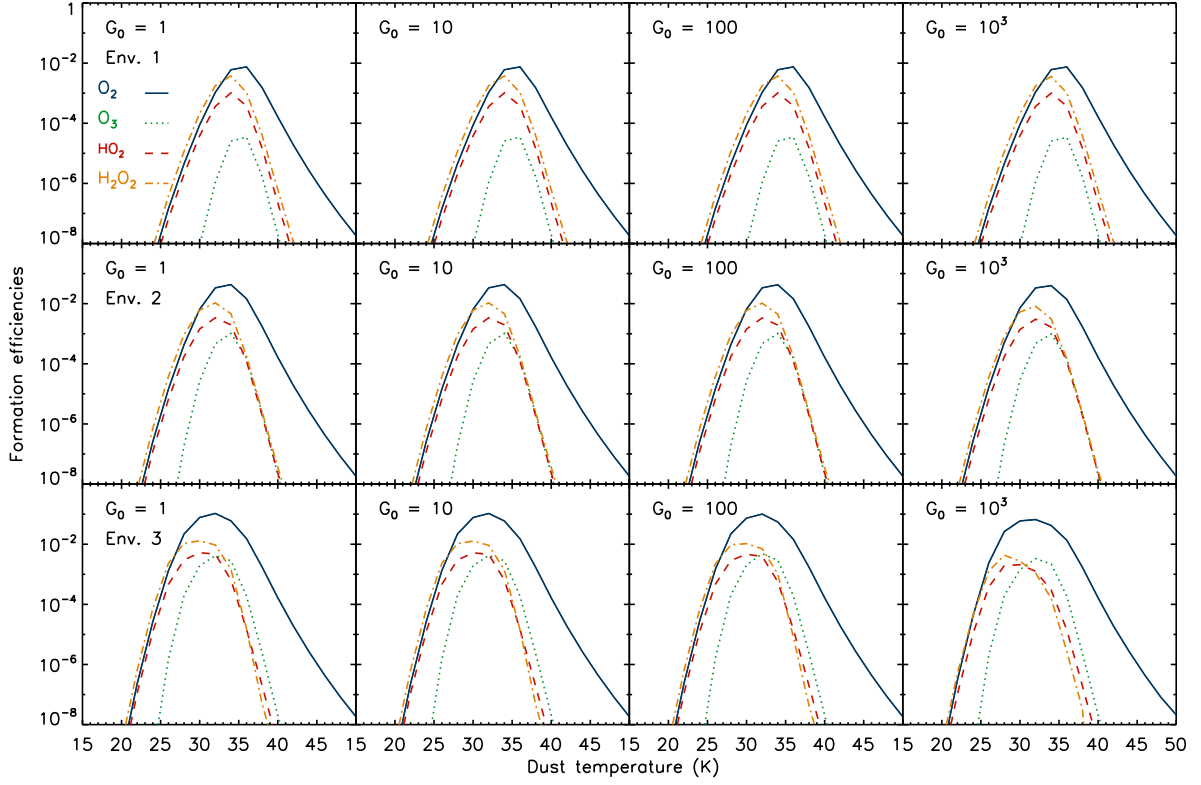


Fig. 4. Efficiencies for the formation of oxygen bearing species O₂, O₃, OH₂, and H₂O₂ in low density gas ($n = 10^3 \text{ cm}^{-3}$), in atomic and molecular hydrogen dominated gas. UV fields ranging from $G_0=1$ to 1000 are considered.

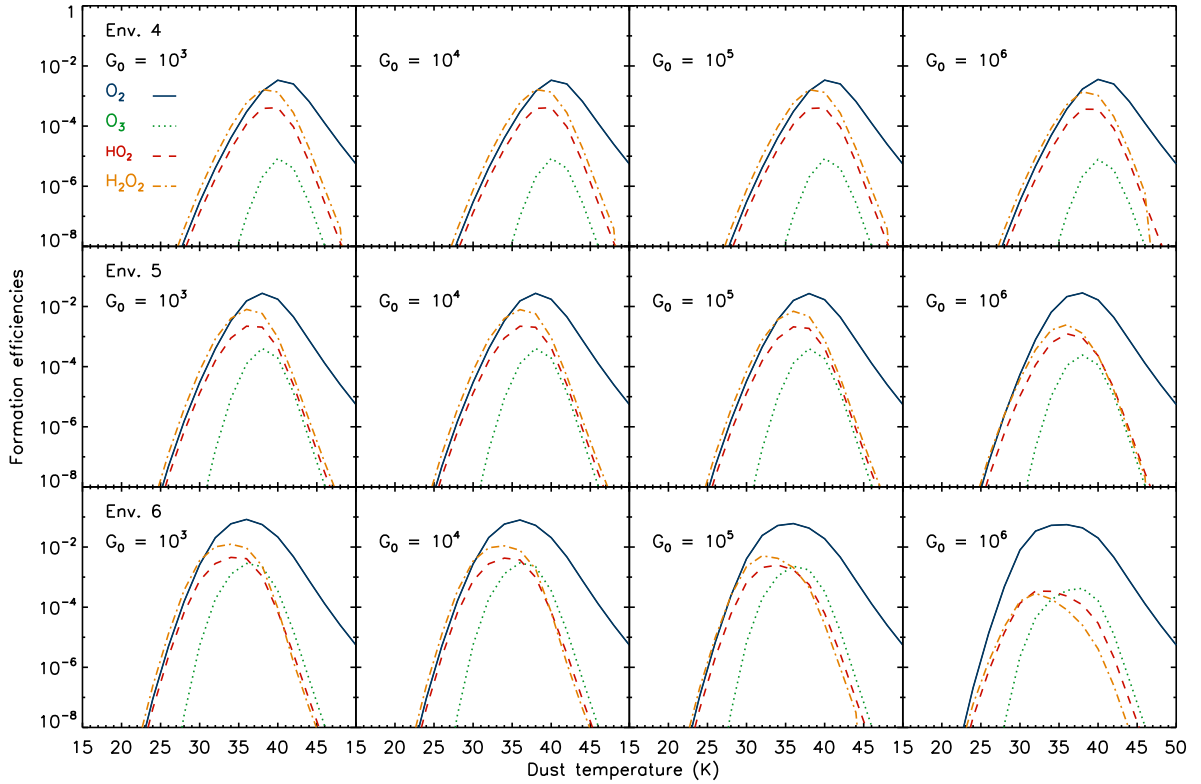


Fig. 5. Efficiencies for the formation of oxygen bearing species O₂, O₃, OH₂, and H₂O₂ in high density gas ($n = 10^{5.5} \text{ cm}^{-3}$), in atomic and molecular dominated gas. UV fields ranging from $G_0 = 10^3$ to 10^6 are considered.

$$\epsilon_{\text{OH}} = \frac{f_{\text{desOH}} n(\text{O}) n(\text{H}) \alpha_{\text{H}}}{R_{\text{acc}}(\text{O})} + \frac{f_{\text{desOH}} n(\text{O}_3) n(\text{H}) \alpha_{\text{H}}}{R_{\text{acc}}(\text{O})} \quad (9)$$

$$\epsilon_{\text{H}_2\text{O}} = \frac{f_{\text{desH}_2\text{O}} n(\text{OH}) n(\text{H}) \alpha_{\text{H}}}{R_{\text{acc}}(\text{O})}. \quad (10)$$

The fractions f_{desOH} , f_{desOH} , and $f_{\text{desH}_2\text{O}}$ are 0.36, 0.25, and 0.15, respectively. These are the fractions of the molecules that are released in the gas phase upon formation due to the exothermicity of the reaction. $R_{\text{acc}}(\text{O})$ is the accretion rate of oxygen, while $n(\text{O})$, $n(\text{O}_3)$, and $n(\text{OH})$ are the dust surface densities of O, O₃, and OH, respectively, in monolayers, e.g., 1 monolayer = 100% coverage. These surface densities are listed in Appendix A. α_{H} is the mobility of hydrogen atoms on the grain surface. The efficiency for the formation of water does *not* contain a term with accretion of OH from the gas phase, since the accretion of O followed by OH formation dominates over OH accretion.

A very important outcome of the simulation is that the formation of OH on grains is dominated by $\text{O} + \text{H} \rightarrow \text{OH}$ up to temperatures $T \sim 30 - 40$ K depending on the environment, and by $\text{O}_3 + \text{H} \rightarrow \text{OH} + \text{O}_2$ at higher temperatures. This implies that apart from expressions for $n(\text{O})$ and $n(\text{OH})$, also those for $n(\text{O}_2)$ and $n(\text{O}_3)$ are needed. For completeness, we also give the one for $n(\text{H}_2\text{O})$. The importance of the $\text{O}_3 + \text{H}$ reactions is shown in Fig. 6. It is obvious from the figure that the OH formation efficiency would be underestimated without the consideration of the reaction with O₃. These results are not inconsistent with those obtained by Ioppolo et al. (2008), where the formation of H₂O is dominated by the reaction sequence: $\text{H} + \text{O}_2 \rightarrow \text{HO}_2$, $\text{H} + \text{HO}_2 \rightarrow \text{H}_2\text{O}_2$ followed by $\text{H} + \text{H}_2\text{O}_2 \rightarrow \text{H}_2\text{O} + \text{OH}$. We do consider the same reaction rate paths in our work, but in this study, molecules are formed on *bare grains*, while Ioppolo et al. (2008) consider *icy grains mantles*. In our simulation a very significant part of the molecules are desorbed upon formation, while the cycle of photodissociation of H₂O and reformation on the grains significantly enhances the amount of water released in the gas phase. *It does not require the complex route through H₂O₂*. There is also another way to form H₂O that involves O₃. The reaction $\text{O} + \text{O}_2 \rightarrow \text{O}_3$, that releases only a very small part into the gas phase upon formation (only a few percent). So although the efficiency for the formation of O₃ is low, there is a significant amount of O₃ on the surface to react to OH. The work by Hollenbach et al. (2009) is also very different from ours. They also treat a surface chemistry network, with H₂, OH, O₂, and some other different species, such as CH, CH₂, and CH₃. They do not include processes with O₃ and H₂O₂, intermediate species in the processes leading to water formation. However, the biggest difference between our models are the *dominant* processes to deliver species back into the gas-phase which are thermal, photo, and cosmic-ray desorption in the Hollenbach et al. (2009) paper, as they are considering ices in that work, whereas this is desorption upon formation in our work. They consider a PDR environment, and therefore they allow for the formation of strongly bound ice-layers. We assume that this does not occur because of the turbulent motions stripping the grains and the strong photodissociating radiation fields that are internally created by X-rays.

The approximate analytical fits to the rate equation results are very good for environments 1, 2, 4 and 5. However, environment 3 and 6, which are highly molecular, start to show deviations for dust temperatures $T_{\text{dust}} > 30$ K for the H₂O. This is due to additional reactions on the grain surface, that we did include in the rate equation method, but not in the approximate fit.

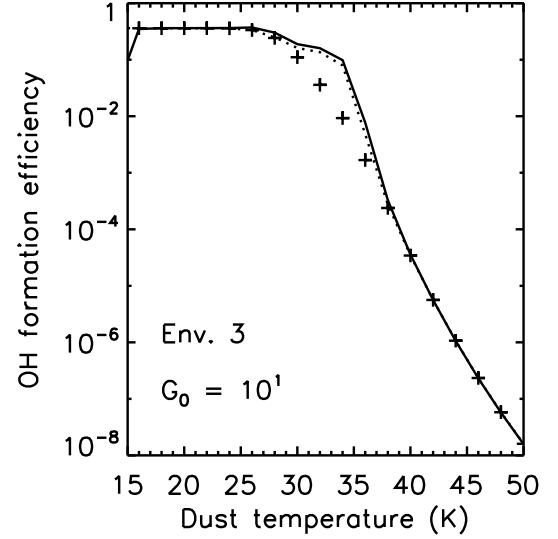


Fig. 6. Efficiencies for environment 3, largely molecular, low density $n = 10^3 \text{ cm}^{-3}$ gas, $G_0 = 10^4$: Result from rate equations simulation (solid line), with (dotted line) and without (crosses) inclusion of the reaction $\text{O}_3 + \text{H} \rightarrow \text{OH} + \text{O}_2$ in the analytical expression.

The fits should not be applied at very low dust temperatures ($T_{\text{dust}} < 10$ K, because the analytical fits do not match the MC and rate equation results.

5. OH and H₂O formation: gas versus dust

In order to estimate the importance of OH and H₂O formation on dust grains, a comparison is made to the gas phase neutral-neutral formation rates which are given by (UMIST database: Le Teuff et al. 2000; Woodall et al. 2007):

$$k_{\text{OH,gas}} = 3.14 \cdot 10^{-13} \left(\frac{T_{\text{gas}}}{300} \right)^{2.70} \exp\left(-\frac{3150}{T_{\text{gas}}}\right) \text{ cm}^3 \text{ s}^{-1} \quad (11)$$

$$k_{\text{H}_2\text{O,gas}} = 2.05 \cdot 10^{-12} \left(\frac{T_{\text{gas}}}{300} \right)^{1.52} \exp\left(-\frac{1736}{T_{\text{gas}}}\right) \text{ cm}^3 \text{ s}^{-1}, \quad (12)$$

while the conservative dust phase reaction rates (using the cross sections from the MRN distribution, $n_{\text{dust}} \sigma / n(\text{H}) = 10^{-21} \text{ cm}^2$), are given by:

$$k_{\text{OH,dust}} = 3.9 \cdot 10^{-17} \sqrt{\frac{T_{\text{gas}}}{100}} \epsilon_{\text{OH}}(T_{\text{dust}}) \text{ cm}^3 \text{ s}^{-1} \quad (13)$$

$$k_{\text{H}_2\text{O,dust}} = 3.9 \cdot 10^{-17} \sqrt{\frac{T_{\text{gas}}}{100}} \epsilon_{\text{H}_2\text{O}}(T_{\text{dust}}) \text{ cm}^3 \text{ s}^{-1}. \quad (14)$$

Depending on the environment (i.e., the ambient atomic and molecular abundances, gas and dust temperature, etc.), OH and H₂O form preferably on the dust grains or in the gas phase:

- Although the efficiency for formation of OH and H₂O on dust is strongly dependent on the dust temperature T_{dust} , the variations with gas temperature T_{gas} at a fixed dust temperature T_{dust} are very modest.

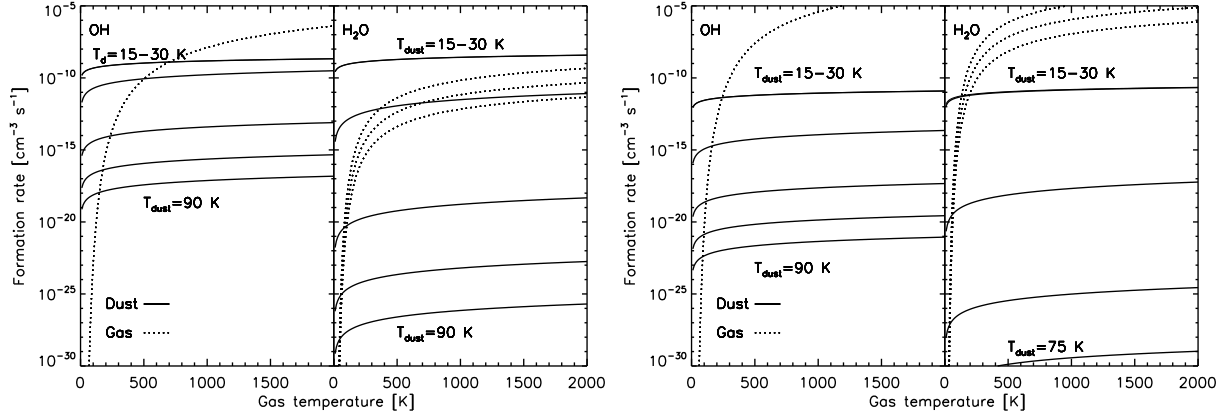


Fig. 7. Comparison of dust and gas phase reaction rates at $n = 10^{5.5} \text{ cm}^{-3}$ for an environment with low (left, $x_{\text{H}} = 1$, $x_{\text{H}_2} = 3 \cdot 10^{-4}$) and high molecular abundances (right, $x_{\text{H}} = 10^{-2}$, $x_{\text{H}_2} = 0.5$) as a function of gas temperature for dust temperatures $T_{\text{dust}} = 15, 30, 45, 60, 75$ and 90 K . The OH abundances are varied between $x_{\text{OH}} = 10^{-8}, 10^{-7}$, and 10^{-6} at low and $10^{-6}, 10^{-5}$, and 10^{-4} at high molecular abundances. This resembles the unshielded and shielded environment of model 4 in Meijerink & Spaans (2005).

- The gas phase formation rates have large activation barriers of $T_{\text{gas}} = 3150$ and 1736 K for the formation of OH and H₂O, respectively. These channels are essentially cut off below temperatures $T_{\text{gas}} \lesssim 200 \text{ K}$.
- Formation on dust depends on abundances of O and H, and in the gas phase on H₂, O, and OH.

For illustration purposes, a comparison between the gas and dust phase formation rates are shown for two different regimes in Fig. 7, a mostly atomic (left) and molecular (right) environment. We do not show the ion-molecule reaction rates, even though they are considered in our chemical network. These processes can be more efficient than the neutral reaction chain at low gas temperatures, which is a domain that we do not consider in this study. The abundances resemble the unshielded and shielded region of model 4 in Meijerink & Spaans (2005) with density $n = 10^{5.5} \text{ cm}^{-3}$: The atomic environment has abundances $x_{\text{H}} = 1$, $x_{\text{H}_2} = 3 \cdot 10^{-4}$, $x_{\text{O}} = 3 \cdot 10^{-4}$, $x_{\text{OH}} = 10^{-8}, 10^{-7}$, and 10^{-6} (left), and the molecular environment has abundances $x_{\text{H}} = 10^{-2}$, $x_{\text{H}_2} = 0.5$, $x_{\text{O}} = 2 \cdot 10^{-4}$, and $x_{\text{OH}} = 10^{-6}, 10^{-5}$, and 10^{-4} (right). We adopt a range of OH abundances, to show the effect on the gas phase rates. We should note here that the OSU astrochemistry database¹ (maintained by Eric Herbst) claims a smaller rate at high temperatures $T > 500$ for the $\text{H}_2 + \text{OH}$ reaction, and is given by $k_{\text{H}_2\text{O,gas}} = 8.4 \times 10^{-13} \exp(-1040/T_{\text{gas}})$. This would make the dust surface reaction even more important.

The efficiencies ϵ_{OH} and $\epsilon_{\text{H}_2\text{O}}$ are reasonably high, ~ 0.3 and ~ 0.6 , respectively, at dust temperatures $T_{\text{dust}} < 40 \text{ K}$. As a result, the H₂O dust formation rate is always dominating the gas phase formation in the atomic environment, while the OH dust formation is more important at temperatures $T_{\text{gas}} < 800 \text{ K}$. Even though OH and H₂O formation efficiencies drop very fast for higher dust temperatures, molecule formation with dust as catalyst will always become dominant below a certain gas temperature. The break even point ranges from $T_{\text{gas}} \sim 100 - 400 \text{ K}$ depending on the dust temperature $T_{\text{dust}} = 45 - 90 \text{ K}$. We should keep in mind though that for $T_{\text{dust}} > 35 - 40 \text{ K}$, the formation rates are overestimated in our model.

This picture is different in a molecular environment. Even when the OH and H₂O formation efficiencies are high ($T_{\text{dust}} < 40 \text{ K}$, gas phase formation is more efficient at gas temperatures

$T_{\text{gas}} > 100 - 200 \text{ K}$. Where in the atomic environment, the OH and H₂O gas phase formation is suppressed by the very low abundances of H₂, the dust phase formation rate is suppressed due to the low accretion rate of atomic hydrogen, which is depleted by two orders of magnitude. In the molecular environment, the formation of water in either dust or gas phase is inefficient through neutral-neutral reactions, and ion-molecule reactions will also contribute significantly or even dominate, through the chain $\text{O}^+ + \text{H}_2 \rightarrow \text{OH}^+ + \text{H}$, $\text{OH}^+ + \text{H}_2 \rightarrow \text{H}_2\text{O}^+ + \text{H}$, $\text{H}_2\text{O}^+ + \text{H}_2 \rightarrow \text{H}_3\text{O}^+ + \text{H}$, followed by recombination $\text{H}_3\text{O}^+ + \text{e}^- \rightarrow \text{H}_2\text{O} + \text{H}$.

6. Application to X-ray environments

The inner regions of active galaxies from, e.g., Mrk 231, which are highly exposed to X-rays, are likely to exhibit enhanced formation of H₂O on dust grains: (i) Dust temperatures are expected to be moderate, $T_{\text{dust}} \sim 20 - 40 \text{ K}$, as the heating of dust is less efficient than by UV; (ii) The dynamical timescales are not very long and shocks are expected to be present, and therefore dust particles are not expected to be or stay covered with ice; (iii) Shocks may even be able to break up grains into smaller particles, therefore enlarging the effective surface of dust, where water is expected to form.

In Fig. 8, the chemical abundances of H, H₂, OH and H₂O and temperatures of an XDR model is shown with density $n = 10^{5.5} \text{ cm}^{-3}$, $F_X = 160 \text{ erg cm}^{-2} \text{ s}^{-1}$, and Solar metallicity, $Z = Z_{\odot}$. Three different cases for the formation of OH and H₂O are considered:

1. Gas phase only: The OH abundance is $x_{\text{OH}} \sim 3 \times 10^{-7}$ at low column densities, rising to $\sim 10^{-5}$ just before the H/H₂ transition, leveling off to 10^{-6} . The H₂O abundance is $x_{\text{H}_2\text{O}} \sim 10^{-10}$ at column densities $N < 10^{22} \text{ cm}^{-2}$. As OH, H₂O becomes more and more abundant toward the H/H₂ transition, and reaches an abundance $x_{\text{H}_2\text{O}} \sim 10^{-6}$ beyond $N_{\text{H}} \sim 10^{23} \text{ cm}^{-2}$.
2. Gas and dust with an MRN distribution: Nothing changes for OH. As shown in Fig. 7, the OH gas phase formation is more important at gas temperatures $T > 800 \text{ K}$, at all dust temperatures. The abundance of H₂O, however, is higher by a factor 8, at low column densities $N_{\text{H}} < 10^{22} \text{ cm}^{-2}$, and thus the

¹ <http://www.physics.ohio-state.edu/~eric/research.html>

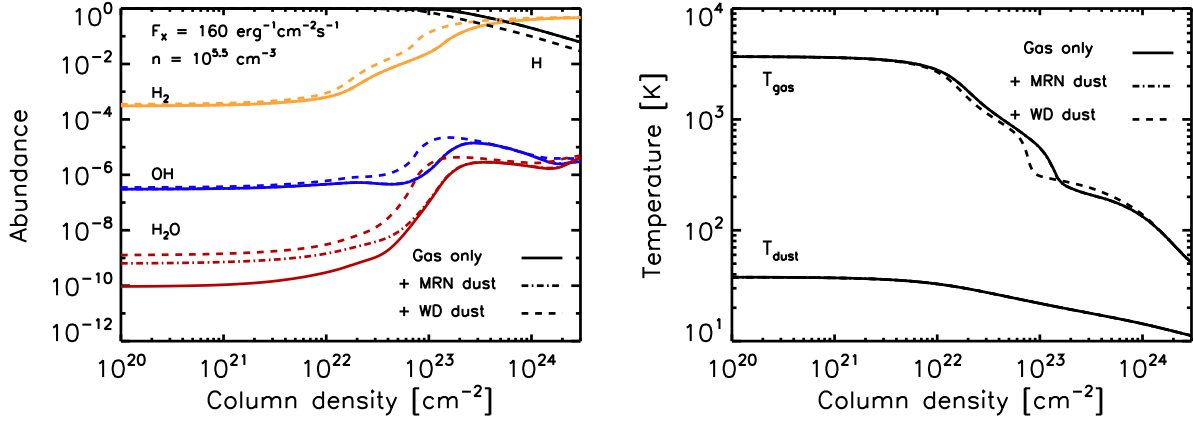


Fig. 8. X-ray irradiated cloud with density $n = 10^{5.5} \text{ cm}^{-3}$ and radiation field $F_X = 160 \text{ erg cm}^{-2} \text{ s}^{-1}$. (*left*) The abundances are shown for H, H₂, OH, and H₂O in three different cases: formation of OH and H₂O (i) in gas phase only (ii) in gas phase and on dust with an MRN size distribution, and (iii) in gas phase and on dust with a Weingartner & Draine size distribution. (*right*) Gas and dust temperatures for the same models. Note that the temperature profiles for the gas only models and those where OH and H₂O formation on dust with an MRN distribution are included are the same.

integrated column of warm water ($T \gtrsim 200 \text{ K}$). At low temperatures (i.e., at high column densities, $N_H \gtrsim 10^{23} \text{ cm}^{-2}$), nothing changes for OH and H₂O, as the formation route is dominated by the ion-molecule reactions.

3. Gas and dust with a Weingartner & Draine distribution: The H₂ formation rate is now higher as well due to the higher surface area of the dust grains. As a result a small increase is seen in the H₂ abundance at low column densities. At the same time, the H/H₂ transition occurs at lower column densities, $N_H \sim 2 \times 10^{23} \text{ cm}^{-2}$, compared to $N_H \sim 3 \times 10^{23} \text{ cm}^{-2}$ compared to the gas phase model. As a result, the OH peaks also at a lower column density, and reaches a slightly higher peak abundance. *The OH enhancement is due to a higher gas phase formation rate, as a result of the higher H₂ abundance, not because of the higher formation rate on dust.* The water abundance in the high temperature range is enhanced by more than an order of magnitude. As the H/H₂ transition occurs at smaller column densities, the rise of the water abundance also occurs at these smaller column densities.

To summarize, we find that the warm H₂O column density is enhanced by approximately an order of magnitude over a column $N_H \sim 5 \cdot 10^{22} \text{ cm}^{-2}$, when including H₂O formation on dust. At larger column densities, where temperatures decrease and the gas becomes molecular, the formation on dust grains does not impact the abundance of H₂O. The OH abundance is only indirectly affected by the higher H₂ formation rate on dust when using the Weingartner & Draine (2001) distribution with the higher dust cross section.

7. Discussion & Conclusions

The role and importance of OH and H₂O formation on dust is investigated. We use both Monte Carlo as well as rate equation simulations to determine the efficiency at which oxygen is converted into OH and H₂O on dust grains. The rate equation method is very fast, and is used to calculate a grid of different environment, low and high density ($n = 10^3$ and $10^{5.5} \text{ cm}^{-3}$), different molecular fractions, radiation fields, and temperatures (see Figs. 2 and 3). The Monte Carlo simulations are used as a consistency check, and as these simulations are fairly slow, efficiencies are only calculated for a limited number of dust temper-

atures. At dust temperatures $T_{\text{dust}} < 35 - 40 \text{ K}$, the Monte Carlo and rate equations method yield the same results, within the uncertainties. At higher dust temperatures, the efficiencies obtained by the two methods start to deviate: the rate equation method systematically obtains larger efficiencies than the MC method. This is where the process of OH and H₂O formation on dust enters the stochastic regime. We fitted analytical expression to the derived results from the rate equations, such that they are easy to implement in any chemistry code. We find that:

- OH formation on grains and release to gas phase is dominated by $\text{O} + \text{H} \rightarrow \text{OH}$ ($T_{\text{dust}} < 35 - 40 \text{ K}$, and by $\text{O}_3 + \text{H} \rightarrow \text{OH} + \text{O}_2$ (for higher dust temperatures). The high dust temperatures results in decreasing hydrogen surface densities, because of the increasing evaporation rates.
- H₂O formation on grains and release to gas phase is dominated by $\text{OH} + \text{H} \rightarrow \text{H}_2\text{O}$.
- The fraction of OH and H₂O that is released in the gas upon formation is of the order of 36% and 9% respectively. However, in strong UV radiation fields, water on the dust can be photo-dissociated, and then reform to water, which then gives another contribution to the gas phase. This loop of forming-dissociating-forming.. increases the effective fraction of H₂O released in the gas by a factor 5.
- A gas and dust phase formation rates comparison (see Fig. 7) shows that formation on dust grains is important for dust temperatures lower than 40 K.

We implemented the analytical expressions for the formation rates in the Meijerink & Spaans (2005) XDR code, and calculated a model with parameters representative for the inner regions of active galaxies. We find that the additional processes enhances the integrated column density of warm water. This increased column helps to explain unusually strong water lines observed for Mrk 231, that has an accreting supermassive black hole with X-ray luminosity $L_X \sim 10^{44} \text{ erg/s}$. This ULIRG shows for example a very high H₂O $2_{02}-1_{11} / \text{CO } J = 8-7$ ratio. These ratios are not observed in typical starforming environments that are mainly exposed to UV only (PDR) environments, such as the one observed in the Orion Bar (Habart et al. 2010) or M82 (Panuzzo et al. 2010), where this ratio is typically an order of magnitude or more smaller than in Mrk 231, and as such these

very bright H₂O lines might be typical for regions that are exposed to high X-ray fluxes, close to the accreting black hole in active galaxies.

Acknowledgements. We thank the anonymous referee for a careful reading of the manuscript and giving a constructive report, that significantly improved the paper.

References

- Akai, Y. & Saito, S. 2003, *Japanese Journal of Applied Physics*, 42, 640
- Andersson, S., Al-Halabi, A., Kroes, G.-J., & van Dishoeck, E. F. 2006, *J. Chem. Phys.*, 124, 064715
- Andersson, S. & van Dishoeck, E. F. 2008, *A&A*, 491, 907
- Bergeron, H., Rougeau, N., Sidis, V., Teillet-Billy, D., & Aguillon, F. 2008, *J. Phys. Chem. A*, 112, 11921
- Boksenberg, A., Carswell, R. F., Allen, D. A., et al. 1977, *MNRAS*, 178, 451
- Braitto, V., Della Ceca, R., Piconcelli, E., et al. 2004, *A&A*, 420, 79
- Cazaux, S., Cobut, V., Marseille, M., Spaans, M., & Caselli, P. 2010, *A&A*, 522, A74+
- Cazaux, S. & Tielens, A. G. G. M. 2002, *ApJ*, 575, L29
- Cazaux, S. & Tielens, A. G. G. M. 2004, *ApJ*, 604, 222
- Cuppen, H. M. & Herbst, E. 2007, *ApJ*, 668, 294
- Cuppen, H. M., Ioppolo, S., Romanzin, C., & Linnartz, H. 2010a, *Physical Chemistry Chemical Physics (Incorporating Faraday Transactions)*, 12, 12077
- Cuppen, H. M., Kristensen, L. E., & Gavardi, E. 2010b, *MNRAS*, 406, L11
- Draine, B. T. 1995, *Ap&SS*, 233, 111
- Fischer, J., Sturm, E., González-Alfonso, E., et al. 2010, *A&A*, 518, L41+
- Galli, D. & Palla, F. 1998, *A&A*, 335, 403
- Glover, S. C. O. 2003, *ApJ*, 584, 331
- González-Alfonso, E., Fischer, J., Isaak, K., et al. 2010, *A&A*, 518, L43+
- Habart, E., Dartois, E., Abergel, A., et al. 2010, *A&A*, 518, L116+
- Hollenbach, D., Kaufman, M. J., Bergin, E. A., & Melnick, G. J. 2009, *ApJ*, 690, 1497
- Hollenbach, D. J. & Tielens, A. G. G. M. 1999, *Reviews of Modern Physics*, 71, 173
- Hornekær, L., Rauls, E., Xu, W., et al. 2006, *Physical Review Letters*, 97, 186102
- Ioppolo, S., Cuppen, H. M., Romanzin, C., van Dishoeck, E. F., & Linnartz, H. 2008, *ApJ*, 686, 1474
- Ioppolo, S., Cuppen, H. M., Romanzin, C., van Dishoeck, E. F., & Linnartz, H. 2010, *Physical Chemistry Chemical Physics (Incorporating Faraday Transactions)*, 12, 12065
- Jelea, A., Marinelli, F., Ferro, Y., Allouche, A., & Brosset, C. 2008, *J. Phys. Chem. A*, 112, 11921
- Katz, N., Furman, I., Biham, O., Pirronello, V., & Vidali, G. 1999, *ApJ*, 522, 305
- Launay, J. M., Le Dourneuf, M., & Zeppen, C. J. 1991, *A&A*, 252, 842
- Le Teuff, Y. H., Millar, T. J., & Markwick, A. J. 2000, *A&AS*, 146, 157
- Lee, G., Lee, B., Kim, J., & Cho, K. 2009, *J. Phys. Chem. C*, 113, 14225
- Maloney, P. R., Hollenbach, D. J., & Tielens, A. G. G. M. 1996, *ApJ*, 466, 561
- Mathis, J. S., Ruml, W., & Nordsieck, K. H. 1977, *ApJ*, 217, 425
- Meijerink, R. & Spaans, M. 2005, *A&A*, 436, 397
- Miyauchi, N., Hidaka, H., Chigai, T., et al. 2008, *Chemical Physics Letters*, 456, 27
- Mokrane, H., Chaabouni, H., Accolla, M., et al. 2009, *ApJ*, 705, L195
- Morisset, S., Aguillon, F., Sizun, M., & Sidis, V. 2004, *J. Chem. Phys.*, 121, 6493
- Neufeld, D. A. & Kaufman, M. J. 1993, *ApJ*, 418, 263
- Neufeld, D. A., Lepp, S., & Melnick, G. J. 1995, *ApJS*, 100, 132
- Nisini, B., Benedettini, M., Giannini, T., et al. 1999, *A&A*, 350, 529
- Panuzzo, P., Rangwala, N., Rykala, A., et al. 2010, *A&A*, 518, L37+
- Papadopoulos, P. P., van der Werf, P., Isaak, K., & Xilouris, E. M. 2010, *ApJ*, 715, 775
- Pirronello, V., Liu, C., Roser, J. E., & Vidali, G. 1999, *A&A*, 344, 681
- Sha, X. 2002, *Surface Science*, 496, 318
- Sha, X., Jackson, B., Lemoine, D., & Lepetit, B. 2005, *J. Chem. Phys.*, 122, 014709
- Sturm, B., Bouwman, J., Henning, T., et al. 2010, *A&A*, 518, L129+
- van der Werf, P. P., Isaak, K. G., Meijerink, R., et al. 2010, *A&A*, 518, L42+
- van Kempen, T. A., Green, J. D., Evans, N. J., et al. 2010, *A&A*, 518, L128+
- Wagner, A. F. & Graff, M. M. 1987, *ApJ*, 317, 423
- Weingartner, J. C. & Draine, B. T. 2001, *ApJ*, 548, 296
- Woodall, J., Agúndez, M., Markwick-Kemper, A. J., & Millar, T. J. 2007, *A&A*, 466, 1197
- Zecho, T., Guttler, A., Sha, X., Jackson, B., & Kuppers, J. 2002, *J. Chem. Phys.*, 117, 8486

Appendix A: OH and H₂O formation efficiencies

The formation efficiency with which gas phase OH and H₂O are formed can be written as a balance between the desorption fraction from the grain upon formation, and the accretion rate of oxygen atoms onto the grain. On grains, two formation processes play a major role for OH in different dust temperature regimes, while for H₂O, there is only one major formation route:



Therefore, the efficiencies should be written as:

$$\epsilon_{\text{OH}} = \frac{f_{\text{desOH}} n(\text{O}) n(\text{H}) \alpha_{\text{H}}}{R_{\text{acc}}(\text{O})} + \frac{f_{\text{desOH}'} n(\text{O}_3) n(\text{H}) \alpha_{\text{H}}}{R_{\text{acc}}(\text{O})} \quad (\text{A.4})$$

$$\epsilon_{\text{H}_2\text{O}} = \frac{f_{\text{desH}_2\text{O}} n(\text{OH}) n(\text{H}) \alpha_{\text{H}}}{R_{\text{acc}}(\text{O})} \quad (\text{A.5})$$

$n(\text{H})$, $n(\text{O})$, $n(\text{O}_3)$, and $n(\text{OH})$ are the surface density of H, O, O₃, and OH on the dust. These hydrogen and oxygen atoms are accreted from the gas phase at a rate:

$$R_{\text{acc}}(\text{H}) = \frac{n_{\text{HI}} v_{\text{HI}}}{N_{\text{S}}} \text{ monolayers } s^{-1}, \quad (\text{A.6})$$

$$R_{\text{acc}}(\text{O}) = \frac{n_{\text{OI}} v_{\text{OI}}}{N_{\text{S}}} \text{ monolayers } s^{-1}, \quad (\text{A.7})$$

where n_{HI} and n_{OI} are the densities of atomic hydrogen and oxygen in the gas phase, v_{HI} and v_{OI} the mean velocities of these atoms:

$$v_{\text{HI}} \sim 1.45 \cdot 10^5 \sqrt{\frac{T_{\text{gas}}}{100}} \text{ cm } s^{-1}, \quad (\text{A.8})$$

$$v_{\text{OI}} \sim 3.6 \cdot 10^4 \sqrt{\frac{T_{\text{gas}}}{100}} \text{ cm } s^{-1}, \quad (\text{A.9})$$

and $N_{\text{S}} = \frac{1}{a_{\text{pp}}} = 8 \cdot 10^{14} \text{ cm}^{-2}$ the number of sites per cm^2 . H atoms arrive on the dust surface in physisorbed sites, and then continue to a chemisorbed site or evaporate from the surface. As a result, the density on the surface can be written as

$$n(\text{H}) = \frac{R_{\text{acc}}(\text{H})}{\alpha_{\text{pc}} + R_{\text{evapH}}} \quad (\text{A.10})$$

The mobility for hydrogen atoms to enter into a chemisorbed site is mostly due to tunneling, which we can then approximate by $\alpha_{\text{pc}} = 10^{12} \exp(-2a_{\text{pc}} \sqrt{\frac{2m_{\text{H}} E_{\text{A}}}{\hbar^2}}) = 6.7 \times 10^{-3}$, where a_{pc} and E_{A} are the width and the height of the barrier between physisorbed and chemisorbed sites. The adopted values are $a_{\text{pc}} = 1.5 \text{ \AA}$ and $E_{\text{A}} = 2870 \text{ K}$. The hydrogen surface density can then be calculated as follows

$$n(\text{H}) = \frac{1.45 \cdot 10^{-10} n_{\text{HI}} \sqrt{\frac{T_{\text{gas}}}{100}}}{6.7 \times 10^{-3} + 10^{12} \exp(-\frac{526}{T_{\text{dust}}})} \quad (\text{A.11})$$

The formation of OH and H₂O can be determined analytically from the rate equations, when the most important processes are considered. The rate equations of O, OH, and H₂O, as well as O₂ and O₃ are considered here, since the efficiency of OH depends on the abundance of O₃ as well. The abundance change as a function of time for these species are given by the following expressions:

$$\frac{dn(\text{O})}{dt} = R_{\text{acc}}(\text{O}) - n(\text{O}) n(\text{H}) \alpha_{\text{H}} + n(\text{OH}) R_{\text{photOH}} - 2n(\text{O})^2 \alpha_{\text{O}} - R_{\text{evapO}} n(\text{O}) \quad (\text{A.12})$$

$$\frac{dn(\text{OH})}{dt} = (1 - f_{\text{desOH}}) n(\text{O}) n(\text{H}) \alpha_{\text{H}} + R_{\text{photH}_2\text{O}} n(\text{H}_2\text{O}) - R_{\text{photOH}} n(\text{OH}) - n(\text{OH}) n(\text{H}) \alpha_{\text{H}} - R_{\text{evapOH}} n(\text{OH}) \quad (\text{A.13})$$

$$\frac{dn(\text{H}_2\text{O})}{dt} = (1 - f_{\text{desH}_2\text{O}}) n(\text{OH}) n(\text{H}) \alpha_{\text{H}} - R_{\text{photH}_2\text{O}} n(\text{H}_2\text{O}) - n(\text{H}_2\text{O}) n(\text{H}) \alpha_{\text{H}} \quad (\text{A.14})$$

$$\frac{dn(\text{O}_2)}{dt} = (1 - f_{\text{desO}_2}) n(\text{O})^2 \alpha_{\text{O}} + (1 - f'_{\text{desO}_2}) n(\text{OH}) n(\text{O}) \alpha_{\text{OH}} - n(\text{O}_2) n(\text{H}) \alpha_{\text{H}} - R_{\text{photO}_2} n(\text{O}_2) - R_{\text{evapO}_2} n(\text{O}_2) \quad (\text{A.15})$$

$$\frac{dn(\text{O}_3)}{dt} = (1 - f_{\text{desO}_3}) n(\text{O}_2) n(\text{O}) \alpha_{\text{O}} - n(\text{O}_3) n(\text{H}) \alpha_{\text{H}} - n(\text{O}_3) n(\text{OH}) \alpha_{\text{OH}} - R_{\text{photo}_3} n(\text{O}_3) \quad (\text{A.16})$$

Table A.1. Adopted photodissociation rates in the approximation

Reaction	Rate (s ⁻¹)
OH + photon → O + H	3.9(-10)
O ₂ + photon → O + O	7.9(-10)
H ₂ O + photon → OH + H	8.0(-10)
O ₃ + photon → O ₂ + O	1.9(-09)

When we consider the surface densities of the species at steady state, the surface densities of the species become

$$n(\text{O}) = \frac{R_{\text{acc}}(\text{O})}{n(\text{H})\alpha_{\text{H}} + R_{\text{evapO}} - R_{\text{photOH}} \frac{1-f_{\text{desOH}}}{f_{\text{desH}_2\text{O}} + \frac{R_{\text{photOH}}}{n(\text{H})\alpha_{\text{H}}}} + \sqrt{2R_{\text{acc}}(\text{O})\alpha_{\text{O}}} \quad (\text{A.17})$$

$$n(\text{OH}) = \frac{(1 - f_{\text{desOH}})n(\text{O})}{f_{\text{desH}_2\text{O}} + \frac{R_{\text{photOH}}}{n(\text{H})\alpha_{\text{H}}} + \frac{R_{\text{evapOH}}}{n(\text{H})\alpha_{\text{H}}}} \quad (\text{A.18})$$

$$n(\text{H}_2\text{O}) = \frac{(1 - f_{\text{desH}_2\text{O}})n(\text{OH})n(\text{H})\alpha_{\text{H}}}{n(\text{H})\alpha_{\text{H}} + R_{\text{photH}_2\text{O}}} \quad (\text{A.19})$$

$$n(\text{O}_2) = \frac{(1 - f_{\text{desO}_2})n(\text{O})^2\alpha_{\text{O}} + (1 - f'_{\text{desO}_2})n(\text{OH})n(\text{O})\alpha_{\text{OH}}}{n(\text{H})\alpha_{\text{H}} + R_{\text{photO}_2} + R_{\text{evapO}_2}} \quad (\text{A.20})$$

$$n(\text{O}_3) = \frac{(1 - f_{\text{desO}_3})n(\text{O}_2)n(\text{O})\alpha_{\text{O}}}{n(\text{H})\alpha_{\text{H}} + n(\text{OH})\alpha_{\text{OH}} + R_{\text{photO}_3}} \quad (\text{A.21})$$

Filling in the equations for the various included reactions, the expressions become as follows:

$$n(\text{O}) = \frac{R_{\text{acc}}(\text{O})}{10^{12} \exp(\frac{-350}{T_{\text{dust}}})n(\text{H}) + 10^{12} \exp(\frac{-1366}{T_{\text{dust}}}) - \frac{3.90 \cdot 10^{-10} G_0 \cdot 0.64}{0.15 + \frac{3.9 \cdot 10^{-10} G_0}{n(\text{H}) \exp(\frac{-350}{T_{\text{dust}}})}} + \sqrt{R_{\text{acc}}(\text{O}) 10^{12} \exp(\frac{-910}{T_{\text{dust}}})}} \quad (\text{A.22})$$

$$n(\text{OH}) = \frac{0.64n(\text{O})}{0.15 + \frac{3.90 \cdot 10^{-10} G_0}{n(\text{H}) 10^{12} \exp(\frac{-350}{T_{\text{dust}}})} + \frac{10^{12} \exp(\frac{-1336}{T_{\text{dust}}})}{n(\text{H}) 10^{12} \exp(\frac{-350}{T_{\text{dust}}})}} \quad (\text{A.23})$$

$$n(\text{H}_2\text{O}) = \frac{0.85n(\text{H})n(\text{OH}) 10^{12} \exp(\frac{-350}{T_{\text{dust}}})}{n(\text{H}) 10^{12} \exp(\frac{-350}{T_{\text{dust}}}) + 8 \cdot 10^{-10} G_0} \quad (\text{A.24})$$

$$n(\text{O}_2) = \frac{0.975n(\text{OH})n(\text{O}) 10^{12} \exp(\frac{-890}{T_{\text{dust}}}) + 0.64n(\text{O}_2) 10^{12} \exp(\frac{-910}{T_{\text{dust}}})}{n(\text{H}) 10^{12} \exp(\frac{-350}{T_{\text{dust}}}) + 7.90 \cdot 10^{-10} G_0 + 10^{12} \exp(\frac{-1416}{T_{\text{dust}}})} \quad (\text{A.25})$$

$$n(\text{O}_3) = \frac{0.977n(\text{O})n(\text{O}_2) 10^{12} \exp(\frac{-910}{T_{\text{dust}}})}{n(\text{H}) 10^{12} \exp(\frac{-350}{T_{\text{dust}}}) + 10^{12} \exp(\frac{-890}{T_{\text{dust}}})n(\text{OH}) + 1.8 \cdot 10^{-10} G_0} \quad (\text{A.26})$$